Patterns of Alluviation in Mixed Bedrock-Alluvial Channels: 1. Numerical Model

Jongseok Cho[1] and Peter A. Nelson[1]

[1]Department of Civil and Environmental Engineering, Colorado State University, Fort Collins, Colorado, USA.

Corresponding author: Peter Nelson (peter.nelson@colostate.edu)

Key Points:

- A new model is developed to predict the dynamics of alluvial patterns in mixed bedrock-alluvial channels.
- The model accurately predicts bedform evolution in an alluvial channel and alluvial patch formation in a mixed bedrock-alluvial channel.
- Accounting for differential roughness and shear stress correction are important for model prediction of the degree of exposed bedrock.

Abstract

Mixed bedrock-alluvial rivers can exhibit partial alluvial cover, which may play an important role in controlling bedrock erosion rates and landscape evolution. However, numerical morphodynamic models generally are unable to predict the pattern of alluviation in these channels. Hence we present a new two-dimensional depth-averaged morphodynamic model that can be applied to both fully alluvial and mixed bedrock-alluvial channels, and we use the model to gain insight into the mechanisms responsible for the development of sediment patches and patterns of bedrock alluviation. The model computes hydrodynamics, sediment transport, and bed evolution, using a roughness partitioning that accounts for differential roughness of sediment and bedrock, roughness due to sediment transport, and form drag. The model successfully replicates observations of bar development and migration from a fully alluvial flume experiment, and it models persistent sediment patches observed in a mixed bedrock-alluvial flume experiment. Numerical experiments in which the form drag, sediment transport roughness, and ripple factor correction were neglected did not successfully reproduce the observed persistent sediment cover in the mixed bedrock-alluvial case, suggesting that accounting for these different roughness components is critical to successfully model sediment dynamics in bedrock channels.

Plain Language Summary

The spatial distribution of sediment patches in bedrock rivers can play an important role in the local hydraulic conditions as well as long-term channel and landscape evolution, because sediment in these channels is an important mechanism of bedrock erosion. Flume experiments and field studies have shown that the amount of sediment cover and the pattern of sediment patches in these streams can sometimes reach a sort of equilibrium, but numerical models have been largely unable to replicate those observations. Here, we present a new numerical model for

mixed bedrock-alluvial rivers that explicitly accounts for different roughness feedbacks between the bedrock, sediment, and flow field. We show that the model can successfully simulate observations from flume experiments conducted with and without exposed bedrock, and it is able to simulate persistent partial sediment cover. These conditions develop because of the complicated roughness feedbacks in these channels, which we demonstrate through simulations where different roughness components are "turned off," which result in completely exposed bedrock without sediment cover.

1 Introduction

River channels can be classified as either alluvial, bedrock, or mixed bedrock-alluvial (Howard, 1980, 1987, 1998; Howard et al., 1994; Knighton, 2014). The beds of alluvial rivers are entirely covered by sediment of sufficient thickness so that the underlying bedrock is not exposed (Tinkler & Wohl, 1998; Whipple, 2004). In contrast, bedrock channels are characterized by frequently exposed bedrock and a lack of continuous alluvial cover in the channel bed and banks. Mixed bedrock-alluvial channels tend to have sediment supply that is less than their sediment transport capacity, and they feature the exposed bedrock interspersed with patches of alluvial cover, potentially taking the form of alternate bars (e.g., Chatanantavet & Parker, 2008) or point bars at meander bends (P. A. Nelson et al., 2014; Nittrouer et al., 2011).

The pattern of alluvial cover in mixed bedrock-alluvial channels likely plays a role in the morphological evolution of those channels, and consequently on landscape evolution (Gasparini et al., 2007; Hodge & Hoey, 2012; Howard et al., 1994; Seidl & Dietrich, 1992; Tinkler & Wohl, 1998; Whipple & Tucker, 2002; Wohl, 1993). Bedrock channel erosion sets the lower boundary condition for landscape evolution and bedrock channels convey climatic and tectonic perturbation through the landscape (Whipple, 2001; Whipple & Tucker, 1999). Alluvial cover is

an important component of mechanistic models of bedrock erosion; for example, the saltation-abrasion model incorporates the erosional mechanism of saltating bedload particles impacting and eroding bedrock (Demeter et al., 2005; Hartshorn et al., 2002; Sklar & Dietrich, 1998, 2001, 2004; Zhang et al., 2015). Competition between the tools and cover effects controls the spatial distribution of the bedrock channel erosion that results in lateral and vertical channel erosion and meandering (Finnegan et al., 2007; Lamb et al., 2015; Turowski et al., 2007; Turowski, Hovius, Meng-Long, et al., 2008; Turowski, Hovius, Wilson, et al., 2008).

Observations from flume experiments documenting the development of alluvial cover patterns on bedrock beds have shown that alluvial cover in these channels depends on channel slope, the initial thickness of alluvial sediment, sediment supply, bedrock roughness, and channel topography. Chatanantavet and Parker (2008) conducted a series of experiments in a straight flume where they varied the rate of sediment supply, the initial cover of sediment on the bed, the slope, and the grain size. Their experiments illuminated several exciting phenomena in mixed bedrock-alluvial channels. First, the pattern and trajectory of the alluvial cover appear to be slope-dependent, wherein at low slopes ($S = 0.0115$) the exposed bed fraction linearly decreases with increasing sediment supply, akin to the linear relationship hypothesized by Sklar and Dietrich (2004). However, at higher slopes ($S = 0.02$), experiments starting with a bare bed did not develop persistent alluvial cover at any supplied rate until that rate exceeded the overall transport capacity of the channel. At that point, "runaway alluviation" occurred, and the entire channel became covered in sediment. Second, the thickness of the initial alluvial cover affected the dynamics of alluviation on the bed, wherein at low initial alluvial thickness the bed was stripped clean, whereas thicker initial sediment covers eventually reached a non-zero fraction of

bedrock exposure. Third, some of their experiments developed continuous strips of sediment moving from one side of the channel to the other, akin to alternate bars.

Other experiments have suggested that bedrock topography and the relative hydraulic roughness of bedrock relative to grain size plays a role in alluvial dynamics of mixed bedrock-alluvial channels. Mishra and Inoue (2020) performed flume experiments with varying bedrock roughness. The observed the extent of alluvial cover increases with increasing sediment supply when the hydraulic roughness of the bedrock bed is larger than that of the alluvial surface. However, a sudden transition from bare bedrock bed to full alluviation was observed as sediment supply momentarily exceeded the channel's transport capacity when the ratio of hydraulic roughness height of bedrock to grain size (k_{sb}/d) is 1.9 or lower. They also proposed an approximation of dimensionless critical shear stress for incipient particle motion over bedrock beds as a function of relative roughness height. Hodge and Hoey (2016a, 2016b) performed experiments in a 3D printed scale model of a jointed limestone bedrock river in which the patterns of sediment deposits at different sediment supply rates were documented. Their experiments pointed out the importance of bedrock topography on depositional patterns, as patches of sediment tended to form in the lowest portions of the bed, and at higher discharge and sediment supply, the bed topography played a less important role than sediment-sediment and sediment-flow interactions in stabilizing patches of alluvium.

Numerical models of sediment transport and bed evolution in mixed bedrock-alluvial channels have struggled to capture the dynamics of alluvial cover observed in experiments or in the field. Morphodynamic models simulate river channel evolution by iteratively using hydraulic flow field calculations to estimate sediment transport rates, which are then used in the conservation of sediment mass (i.e., the Exner equation) to calculate bed erosion and deposition

patterns. These types of models have been used for decades to understand the dynamics of alluvial rivers, such as the development and migration of alternate bars (e.g., Bernini et al., 2006; Defina, 2003; Qian et al., 2017), sediment sorting (e.g., P. A. Nelson et al., 2015a, 2015b), braiding (e.g., Murray & Paola, 1997; Schuurman et al., 2013), meandering (e.g., Smith & Mclean, 1984; J. M. Nelson et al., 2003), and armoring (e.g., Parker & Klingeman, 1982; Parker & Toro-Escobar, 2002). However, alluvial morphodynamic models generally assume that the sediment supply equals or exceeds the sediment transport capacity, which is not the case for mixed bedrock-alluvial rivers.

This assumption has only recently begun to be relaxed in attempts to use morphodynamic models to better understand mixed bedrock-alluvial rivers (e.g., P. A. Nelson & Seminara, 2012). Using a cellular automaton model governed by probabilities of individual grain movement, Hodge and Hoey (2012) studied the relationship between the fraction of bedrock exposure and the ratio of sediment supply to capacity on noneroding bedrock beds. Zhang et al. (2015) expressed bedrock cover fraction as a ratio of vertical length scale between alluvial thickness and macro-roughness of bedrock topography representing the statistical characteristics of bedrock surface fluctuations. This MRSAA (Macro-Roughness-based Saltation-Abrasion-Alluviation) model was later implemented to investigate the knickpoint migration (Zhang et al., 2018, 2019) and formation of the cyclic steps (Izumi et al., 2017) to spatiotemporal variation of sediment supply. Inoue et al. (2016) provided an early attempt to investigate alternate bar formation and bedrock incision in mixed bedrock-alluvial channels in response to the different ratio of sediment supply to channel's transport capacity.

Larger-than-grain-scale bedrock topography, sometimes called "macrotopography", has recently been incorporated into one-dimensional morphodynamic models (Zhang et al., 2015).

128 The model solutions for alluvial response to sediment supply show that stripping of antecedent
129 sediment from upstream to downstream occurs with the termination of sediment supply, and the
130 development of an alluvial layer with a thickness corresponding to the ratio of sediment supply
131 to transport capacity (q_s/q_c), which propagates downstream over bare bedrock when the
132 sediment supply is increased. Application of nonlinear wave speed to the alluvial layer predicted
133 that alluvium over a bedrock surface with a small cover fraction migrated downstream much
134 faster than those consisting of a higher fraction cover.

135 Despite these recent advances in modeling the morphodynamics of mixed bedrock-
136 alluvial rivers, there remain uncertainties about how differences in sediment and bedrock
137 roughness influence in mixed bedrock-alluvial rivers, and how hydraulics and macroroughness
138 features may interact to control alluvial patterns. Existing models are not able to resolve these
139 issues because either they are one-dimensional and unable to predict lateral variation in alluvial
140 cover, or they do not fully account for roughness effects of local sediment cover or transport. For
141 example, current models of mixed bedrock-alluvial morphodynamics have not been able to
142 predict persistent longitudinal alluvial strips, or to fully replicate the relationship between overall
143 sediment cover and the sediment supply to capacity ratio as reported in Chatanantavet and Parker
144 (2008).

145 This study intends to resolve the limitations models encounter when attempting to
146 simulate sediment dynamics in a mixed bedrock-alluvial channel by developing a new model
147 that uses: (1) a two-dimensional approach to account for the influence of potential bedforms
148 (e.g., alternate bars, antidunes, and dunes) in a straight channel; (2) the effect of flow resistance
149 partitioned into skin friction due to stationary particles and bedrock surface roughness, form drag
150 associated with dimensions of alluvial cover and irregular bedrock topography, and bedload

roughness produced by saltating sediment; (3) application of a ripple factor to take into account for an intermediate state between the planar bed and small-scale bedforms.

We hypothesize that accounting for differential bedrock and sediment roughness, roughness from sediment transport, form drag, and a near-bed shear stress correction are necessary to capture sediment dynamics in mixed bedrock-alluvial channels. We use two experiments to demonstrate that our model can reproduce observations made in fully alluvial and mixed bedrock-alluvial channels, and we explore the importance of the different roughness terms we include by repeating the simulation with those terms neglected. We simulate an experiment of Lanzoni (2000) for alternate bar formation in an alluvial channel and an experiment of Chatanantavet and Parker (2008) for gravel patch development in a mixed bedrock-alluvial channel to assess model performance. Our model successfully replicates sediment dynamics in both experiments. The numerical experiments that neglect form drag and transport components of the roughness do not reproduce observations from the Chatanantavet and Parker (2008) experiment, indicating that those components play a critical role in mixed bedrock-alluvial sediment dynamics.

2 Morphodynamic model

We have developed a new morphodynamic model that simulates sediment transport and deposition in mixed bedrock-alluvial channels. This model consists of three components: a hydrodynamic model describing the depth-averaged flow field, a sediment transport model describing bedload sediment transport rate, and a bed evolution model updating bed elevation and the areal fraction of bedrock cover. Unlike previous models of mixed bedrock-alluvial morphodynamics, this new model accounts for form drag and sediment transport roughness, in addition to surface (grain and bedrock) roughness and a roughness-dependent critical Shields

174 stress. In addition, the total shear stress is corrected with a ripple factor in the sediment transport
175 model, as the bedform drag does not contribute to the bedload transport.

176 2.1 Flow model

177 The governing equations for calculating flow depth and velocity are composed of the
178 depth-averaged form of mass continuity and momentum balance in a 2D Cartesian coordinate
179 system:

180 $$\frac{\partial Q}{\partial t}+\frac{\partial F_x}{\partial x}+\frac{\partial F_y}{\partial y}=\frac{\partial D_x}{\partial x}+\frac{\partial D_y}{\partial y}+S_b+S_f \quad (1)$$

181 where t is time, x and y are Cartesian coordinates, Q are the conservative variables, F_x and
182 F_y are the convective fluxes, D_x and D_y are the diffusive fluxes, S_b are the bed slope terms,
183 and S_f are the friction slope:

$$Q=\begin{bmatrix} h \\ hu \\ hv \end{bmatrix},\quad F_x=\begin{bmatrix} hu \\ huu+\frac{1}{2}g\left(h^2-z_b^2\right) \\ hvu \end{bmatrix},\quad F_y=\begin{bmatrix} hv \\ huv \\ hvv+\frac{1}{2}g\left(h^2-z_b^2\right) \end{bmatrix},$$

$$D_x=\begin{bmatrix} 0 \\ 2h\left(\nu+\nu_t\right)+\frac{\partial u}{\partial x} \\ h\left(\nu+\nu_t\right)+\left(\frac{\partial u}{\partial y}+\frac{\partial v}{\partial x}\right) \end{bmatrix},\quad D_y=\begin{bmatrix} 0 \\ h\left(\nu+\nu_t\right)+\left(\frac{\partial u}{\partial y}+\frac{\partial v}{\partial x}\right) \\ 2h\left(\nu+\nu_t\right)+\frac{\partial v}{\partial y} \end{bmatrix},$$

$$S_b=\begin{bmatrix} 0 \\ -g\eta\frac{\partial z_b}{\partial x} \\ -g\eta\frac{\partial z_b}{\partial y} \end{bmatrix},\quad S_f=\begin{bmatrix} 0 \\ -\frac{\tau_{bx}}{\rho} \\ -\frac{\tau_{by}}{\rho} \end{bmatrix}, \tag{2}$$

where h is the flow depth, u and v are the velocities in x- and y-directions, respectively, g is the gravitational acceleration, ν and ν_t are the kinematic viscosity of water and the turbulent eddy viscosity, respectively, η is the water surface elevation, z_b is the bed elevation, and ρ is the density of water. The bed shear stresses τ_{bx} and τ_{by} in x- and y-direction are given by

$$\left(\tau_{bx},\tau_{by}\right)=\rho C_f\sqrt{u^2+v^2}\left(u,v\right) \tag{3}$$

where C_f is a friction coefficient estimated using the law of the wall as a function of the flow depth h and total roughness height k_0:

$$C_f=\left[\frac{1}{\kappa}\ln\left(\frac{11h}{k_0}\right)\right]^{-2}. \tag{4}$$

193 2.2 Depth-averaged mixing-length model

194 The calculation of the turbulent viscosity term is based on a mixing-length model with
195 depth-averaged terms developed by Stansby (2003):

196 $$\nu_t = \sqrt{l_h^4 \left[2\left(\frac{\partial u}{\partial x}\right)^2 + 2\left(\frac{\partial v}{\partial y}\right)^2 + \left(\frac{\partial v}{\partial x} + \frac{\partial u}{\partial y}\right)^2 \right] + \left(\gamma u_* h\right)^2} \quad (5)$$

197 where l_h is a horizontal mixing length scale ($l_h \approx 0.267\kappa h$), κ is the von Karman constant (
198 $\kappa \approx 0.408$), and γ is a constant that accounts for vertical mixing ($\gamma \approx 0.067$). The local shear
199 velocity, u_*, is defined as;

200 $$u_* = \sqrt{\tau_b / \rho} \quad (6)$$

201 where $\tau_b = \sqrt{\tau_{bx}^2 + \tau_{by}^2}$ is the local bed shear stress vector, with components τ_{bx} and τ_{by} in the x-
202 and y-directions, respectively.

203 2.3 Bed roughness

204 The total roughness height k_0 is partitioned into three fractional roughness components,
205 including skin friction k_s, form drag k_f, and bedload transport k_t:

206 $$k_0 = k_s + k_f + k_t . \quad (7)$$

207 The skin friction is induced by the viscous shear stress and pressure force acting on the
208 individual grains on the bed, and it relates to the size of the bed material. The local skin friction
209 roughness height varies with surface particle size in the completely alluvial channel and the
210 degree of irregularity of the bed surface in the bedrock channel. The calculation of skin friction

in the mixed bedrock-alluvial channel is based on the assumption that the skin friction is linearly associated with the changes in the fraction of bedrock covered by alluvium:

$$k_s = P_c k_{sa} + \left(1 - P_c\right) k_{sb} \tag{8}$$

where k_{sa} and k_{sb} are the hydraulic roughness height of the alluvial bed and bedrock bed, respectively. The local areal fraction of alluvial cover $P_c = \eta_a / C_m \le 1$, in which $C_m = \pi d/6$ is the maximum volume of a monolayer of spherical sediment grains of constant diameter d uniformly distributed over the bed surface (P. A. Nelson & Seminara, 2012), and η_a is the thickness of the alluvial layer.

The form drag component of roughness results from the pressure force acting over entire bedforms and is not responsible for the bedload motion of sediment particles (Maddux, McLean, et al., 2003; Maddux, Nelson, et al., 2003). We calculate the form drag component of roughness as a function of bed morphology through the empirical relation of Grant and Madsen (1982):

$$k_f = 30 a_r \frac{\eta_r^2}{\lambda_r} \tag{9}$$

where η_r and λ_r are bed form height and wavelength, and a_r is a coefficient in the range from 0.3 to 3. Grant and Madsen (1982) suggested $a_r = 0.923$, which we use here.

For the sediment transport component of roughness, Wiberg and Rubin (1989) proposed for the flat bed condition:

$$k_t = 30 \alpha_{ws} d \frac{a_1 T_*}{1 + a_2 T_*} \tag{10}$$

where $T_* = \tau^* / \tau_c^*$ is the transport stage, τ^* is the dimensionless shear stress, τ_c^* is the critical dimensionless Shields stress, $a_1 = 0.68$, $a_2 = 0.0204\left(\ln 100d\right)^2 + 0.0220\left(\ln 100d\right) + 0.0709$, and $\alpha_{ws} = 0.056$. Here, the effect of local variation of bed topography is applied to the critical bed shear stress to account for the gravity effect, as described in Section 2.5.

2.4 Bed deformation model

The local volumetric concentration of sediment per unit area is calculated using the sediment conservation model for mixed bedrock-alluvial channel beds proposed by Luu, Egashira, and Takebayashi (2004):

$$\frac{\partial V_{ba}}{\partial t} + \frac{\partial q_{bx}}{\partial x} + \frac{\partial q_{by}}{\partial y} = 0 \tag{11}$$

where V_{ba} is the total volume of sediment per unit area and q_{bx} and q_{by} are vectors of the bedload transport rate per unit width in the x- and y-directions, respectively. The thickness of the alluvial layer η_a and the volume of sediment in the bedload layer V_b are separately updated considering the saturation volume of the bedload layer V_{bc}. This saturation volume is a threshold value that determines whether the particles deposit on the bed or rapidly saltate over the surface without resting on the bed. When V_{ba} exceeds V_{bc}, a volume of sediment equal to the difference between V_{ba} and V_{bc} deposits on the bed as an alluvial layer. When V_{ba} is less than V_{bc}, the particles pass over the bedrock surface as throughput load without deposition:

$$\eta_a = \begin{cases} \dfrac{V_{ba} - V_{bc}}{1 - \lambda} & \text{for} \quad V_{bc} \le V_{ba} \\ 0 & \text{for} \quad 0 \le V_{ba} < V_{bc} \end{cases} \tag{12}$$

where λ represents the porosity of the bed and V_{bc} is the saturation volume of the bedload layer per unit area. When the bedrock is wholly exposed ($\eta_a = 0$), the volume of the throughput bedload layer is lower than the saturation volume. When the bed is partially or fully covered with sediment ($\eta_a > 0$), V_b equates to V_{bc} because sediment particles exchange occurs between alluvial and bedload layers:

$$V_b = \begin{cases} V_{bc} & \text{for} \quad V_{bc} \le V_{ba} \\ V_{ba} & \text{for} \quad 0 \le V_{ba} < V_{bc} \end{cases}. \tag{13}$$

The saturation volume of bedload per unit area V_{bc} is defined by

$$V_{bc} = \frac{q_{bc}}{u_s}, \tag{14}$$

where q_{bc} is the bedload transport capacity per unit width and u_s is the saltation velocity, calculated here with the empirical excess shear stress relation presented in (Sklar & Dietrich, 2004):

$$\frac{u_s}{\sqrt{R_b g d}} = 1.56\left(\frac{\mu\tau^*}{\tau_c^*} - 1\right)^{0.56} \tag{15}$$

where $R_b = \left(\rho_s - \rho\right)/\rho$ denotes submerged specific gravity of sediment and ρ_s is the density of the sediment. The bedload transport capacity per unit width q_{bc} is estimated using the relation based on Ashida and Michiue (1972):

$$\frac{q_{bc}}{\sqrt{R_b g d^3}} = 17\left(\sqrt{\mu\tau^*} - \sqrt{\tau_c^*}\right)\left(\mu\tau^* - \tau_c^*\right) \tag{16}$$

where dimensionless shear stress τ^* is defined as

$$\tau^* = \frac{\tau_b}{\rho R_b g d} \tag{17}$$

and $\mu \le 1$ is the ripple factor, the ratio of the grain roughness to bed roughness (Ribberink, 1987) (discussed further in Section 2.5).

The volumetric sediment transport rate per unit width in the x- and y-directions is denoted

$$\left(q_{bx}, q_{by}\right) = q_b \left(\cos\alpha, \sin\alpha\right) \tag{18}$$

where α is the angle of bedload transport and the sediment transport intensity, q_b, depends on the ratio of the volume of sediment and its saturation value. The bedload transport rate in bedrock with a sufficient local volume of sediment equals the sediment transport capacity. However, in bedrock rivers without sediment cover, the bedload transport rate is less than the bedload transport capacity:

$$q_b = \begin{cases} \dfrac{V_b}{V_{bc}} q_{bc} & \text{for} \quad 0 \le V_b < V_{bc} \\ q_{bc} & \text{for} \quad V_{bc} \le V_b \end{cases}. \tag{19}$$

When considering the effect of gravity acting on particles for gradually varying bed elevation, the sediment transport direction deviates from the direction of the boundary shear stress. Here we adopt the well-known relationship (Struiksma, 1985):

$$\tan\alpha = \frac{\sin\delta - \dfrac{1}{\mathrm{f}\left(t^*\right)} \dfrac{\partial z_b}{\partial y}}{\cos\delta - \dfrac{1}{\mathrm{f}\left(t^*\right)} \dfrac{\partial z_b}{\partial x}} \tag{20}$$

where δ is the near-bed flow direction estimated to account for the influence of spiral water motion induced by bed topography as

$$\delta = \tan^{-1}\left(\frac{v}{u}\right) - \tan^{-1}\left(A\frac{h}{r_s}\right), \tag{21}$$

where the local radius of depth-averaged stream curvature is

$$r_s = \frac{U^3}{u^2\frac{\partial v}{\partial x} + uv\left(\frac{\partial v}{\partial y} - \frac{\partial u}{\partial x}\right) - v^2\frac{\partial u}{\partial y}}, \tag{22}$$

where $U = \sqrt{u^2 + v^2}$ is the local flow velocity and the coefficient weighting the intensity of helical flow is

$$A = \frac{2}{\kappa^2}\left(1 - \frac{\sqrt{C_f}}{\kappa}\right), \tag{23}$$

and $\mathrm{f}\left(\tau^*\right)$ is a function weighting the influence of the bed slope, following the form proposed by Talmon, Struiksma, and Van Mierlo et al. (1995):

$$\mathrm{f}\left(\tau^*\right) = 9\left(\frac{d}{h}\right)^{0.3}\sqrt{\tau^*}\,. \tag{24}$$

2.5 Shear stress correction

The bedload sediment transport rate is expressed as a function of shear stress acting over the channel bed. The presence of bedforms leads to a partial reduction of the total shear stress related to the form drag, and the remainder is available for sediment transport. Traditionally this has been implemented in models by multiplying the dimensionless shear stress by a so-called

296 "ripple factor." Several models for estimating the ripple factor have been proposed as a function
297 of the skin friction relative to the total friction (Ribberink, 1987; Vermeer, 1986):

298 $$\mu = \left(\frac{C_{fs}}{C_f} \right)^{n/2} \tag{25}$$

299 where C_{fs} is the friction coefficient accounting for skin friction obtained by substituting k_0 with
300 $k_s + k_t$ in equation (4), and the exponent n is defined by

301 $$n = 1.8 + 0.27 \log q^*, \tag{26}$$

302 where $q^* = q_{bc} \Big/ \sqrt{R_b g d^3}$ is the dimensionless bedload transport rate. This relationship is valid for
303 $0.001 \le q^* \le 1$ (Vermeer, 1986).

304 2.6 Critical dimensionless Shields stress

305 Flume experiments conducted in bedrock channels (Inoue et al., 2014; Mishra & Inoue,
306 2020) have related the channel roughness and dimensionless critical shear stress of sediment
307 movement. A power approximation proposed by Mishra and Inoue (2020) is applied to this
308 model to take into account the effect of total hydraulic roughness on critical shear stress:

309 $$\tau_{c0}^* = \tau_{c\alpha}^* \left(k_s / d \right)^{0.6} \tag{27}$$

310 where $t_{c\alpha}^*$ is the critical Shields stress back-calculated from sediment transport capacity
311 measured from the experiment in the flat channel. In addition to the bed roughness, the local bed
312 slope effect on the initiation of particle motion can be added because the local bed slope provides
313 a gravitational component of the force exerted on the particle (Duan & Julien, 2005; Soulsby,
314 1997):

315 $$\frac{\tau_c^*}{\tau_{c0}^*} = \frac{\sin(\phi + \beta_s)}{\sin\phi} \frac{\cos\beta_n}{\sqrt{1 - \tan^2\beta_n / \tan^2\phi}} \quad (28)$$

316 where ϕ is the grain angle of repose and β_s and β_n are the slope in the streamwise and cross-
317 stream direction of the sediment transport, respectively. A simple approach was proposed by
318 Wiberg and Smith (1987) for the treatment of heterogeneous bed conditions through the
319 geometric relation of friction angle as a function of particle size to the roughness length scale of
320 the bed:

321 $$\phi = \cos^{-1}\left(\frac{d/k_s - 0.02}{d/k_s + 1}\right) \quad (29)$$

322 The bed slopes in the streamwise and cross-stream direction of sediment transport are

323 $$\beta_s = \tan^{-1}\left(\frac{\partial z}{\partial x}\cos\alpha + \frac{\partial z}{\partial y}\sin\alpha\right), \quad \beta_n = \tan^{-1}\left(\frac{\partial z}{\partial y}\cos\alpha - \frac{\partial z}{\partial x}\sin\alpha\right). \quad (30)$$

324 2.7 Solution procedure

325 The model uses a decoupled approximation of the morphodynamic system by assuming
326 that the response time of the bed evolution is relatively long compared to the time scale of the
327 hydraulic processes (De Vries, 1965; Defina, 2003; J. M. Nelson & Smith, 1989). Therefore the
328 hydrodynamic solver is followed by the calculation of the modified Exner equation.

329 First, local water depth and flow velocity are calculated using the hydrodynamic model
330 (equation (1) - (2)). The friction term is estimated by taking into account the roughness of the
331 bedrock k_{sb} and alluvial surfaces k_{sa}, topographic variability k_f, and the effect of saltating
332 grains during sediment transport k_t. Flow-conservative variables (h, hu, and hv) at each cell

interface are calculated using the total variation diminishing (TVD) scheme (Toro, 2009) for cell-centered advection terms (F_x and F_y).

Second, the local sediment transport rate q_b (equation (19)) is estimated considering the local circumstance of sediment deposition, which is determined by the fraction of bedrock cover P_c (equation (14) - (16)). The depth-averaged flow variables (h , u , v, and k_s) determine the threshold of incipient sediment motion (τ^* and τ_c^*), then the local bedload transport rate q_b , grain saltation velocity u_s , and saturation volume of the bedload layer V_{bc} are calculated.

Third, the sediment flux divergence updates the total sediment volume per unit area (equation (11)). Finally, the new alluvial layer thickness η_a and the volume of bedload transport per unit area V_b are determined by whether the bedrock is covered by alluvium or exposed (equation (12) - (13)).

3 Model validation

We set up two simulations to demonstrate the model's ability to replicate observations in both alluvial and mixed bedrock-alluvial conditions. These benchmark laboratory flume experiments documented: (1) the development of alternate bars in fully alluvial channels (Lanzoni, 2000); and (2) flow and sediment transport in mixed bedrock-alluvial channels (Chatanantavet & Parker, 2008). Table 1 summarizes the conditions for each experiment.

3.1 Alternate bar formation in an alluvial channel

To demonstrate alternate bars in alluvial conditions, we simulate Run P1505 described in Lanzoni (2000). In the experiment, a straight, flow- and sediment-recirculating flume 1.5 m

353 wide, 1 m deep with a 55 m long test section was supplied with a steady water discharge of 30
354 l/s. The bed was composed of a uniform sand size of 0.48 mm and initially screeded flat. At the
355 upstream end of the channel, a 16 m long, 5 m wide stilling basin was installed to ensure smooth
356 and regular water and sediment discharge into the experimental channel. This experiment
357 stopped as it reached equilibrium after 28 hours, when the water surface slope matched the bed
358 slope. A summary of reach-averaged measurements is reported in Table 1. Alternate bars were
359 formed with an average height of 7 cm, wavelength of 10 m, and celerity of 2.80 m/h.

360 Our simulation of Run P1505 is conducted with some modification of experimental
361 conditions. First, a longer channel of 120 m was used to ensure the bar reached the equilibrium
362 state before migrating out of the domain (Defina, 2003). Second, a small topographic bump 0.6
363 m long, 0.75 m wide, and 5 mm high was introduced near the upper boundary on the left side
364 (looking downstream) to create an initial disturbance to induce free bar development because the
365 arbitrarily distributed source of disturbances from the physical experiment was unknown.
366 Numerical models generally require perturbations such as a topographic bump (Defina, 2003;
367 Wu et al., 2011) or a bend upstream of the straight channel (Mendoza et al., 2017) to develop

Table 1. Summary of Experimental Conditions.[a]

	m	m	%	l/s	g/s	mm	cm	m/s	hr
Run	B	L	S	Q_w	Q_c	D	H	U	t
P1505[b]	1.5	55	0.452	30	28	0.48	4.4	0.45	28
2-B2[c]	0.9	13	2	55	110	7	5.5	1.02	5

[a] B is the channel width, L is the channel length, S is the channel slope, Q_w is the water discharge, Q_c is the sediment transport capacity, D is the grain size, H is the averaged flow depth, U is the averaged flow velocity, and t is the duration of the experiment.
[b] Run P1505 was performed by Lanzoni (2000).
[c] Run 2-B2 ($q_s/q_c = 0.56$) was performed by Chatanantavet & Parker (2008).

368 bars in uniform flow over flat-bed conditions. Third, the constant and uniform water discharge
369 and sediment feed rate were imposed at the inlet.

370 3.2 Patterns of bedrock alluviation with limited sediment supply

371 The second experiment Run 2-B2 ($q_s/q_c = 0.56$) (Chatanantavet & Parker, 2008), was
372 carried out on a non-erodible bedrock surface in a 13 m long and 0.9 m wide straight, rectangular
373 flume channel with a slope of 0.02. The bedrock bed was randomly abraded with a longitudinally
374 averaged standard deviation of 2.4 mm, and the distance between the lowest and highest points
375 of the profile is approximately 1 cm (Figure 1b and 3b in Chatanantavet & Parker, 2008).

376 The averaged values of initial experimental conditions are presented in Table 1. The
377 representative hydraulic roughness of the bedrock surface was back-calculated from the
378 Manning-Strickler relation under the flow conditions measured from the experimental results
379 conducted in the channel slope of 0.0115. Initially, the bed was covered entirely with a 2 cm
380 thick layer of uniform 7 mm sediment. The steady water discharge was 55 l/s, the constant
381 sediment supply rate was 62 g/s, and the sediment transport capacity was estimated at 110 g/s for
382 a wholly covered bed. The experiment stopped when the fraction of bedrock cover P_c reached a
383 steady state whose value was approximately 0.59.

384 The numerical model simulation of this experiment uses a 0.9 m wide, 20 m long bedrock
385 bed with randomly generated topographic perturbations with a standard deviation of 2.2 mm and
386 a peak-to-peak distance of bed elevation of 0.9 cm (Figure 1). The roughness height due to skin
387 friction (grain equivalent roughness height) used in the numerical simulation was back calculated
388 from equation (4) using experimentally measured average flow conditions for each case of bare
389 bedrock bed k_{sb} and alluvial bed k_{sa}. In the channel fully covered with sediment $H = 0.06$ m

and $U = 1.02$ m/s, and in case of flow over bare bedrock bed $H = 0.05$ m and $U = 1.22$ m/s, hence k_{sa}=7 mm and k_{sb} = 3 mm. The sediment supply to transport capacity ratio q_s/q_c is 0.6, which means the steady sediment supply rate is 66 g/s assuming the sediment transport capacity of the alluvial bed is 110 g/s. A small perturbation was given by changing sediment distribution patterns at the upstream end of the channel to prevent sediment and bedform from washing out from the upstream end of the channel (e.g., Figure 14 in Inoue et al., 2016).

3.3 Simulations investigating impacts of roughness components on mixed bedrock-alluvial sediment dynamics

To investigate the importance of different roughness components on the model's performance of predicting alluvial patterns, we conducted numerical simulations without bedform roughness or ripple factor under the same conditions of Run 2-B2. The form drag effect on the flow is removed by setting the bedform roughness to zero; hence the ripple factor is no longer influential. The effect of bed-form solely on sediment transport is removed by setting the ripple factor to unity.

We also conducted a simulation where the sediment transport roughness was set to zero, to explore how that component influences morphodynamic predictions in mixed bedrock-alluvial channels. For this simulation, the total roughness consisted of bedform and grain roughness, the latter of which was increased relative to the base scenario so that overall flow depths and velocities still matched experimental observations.

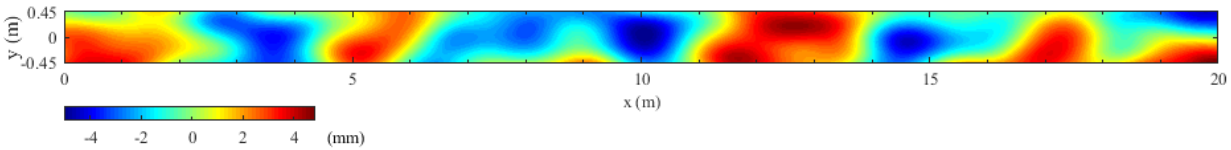

Figure 1. Plan view of bedrock topography. Colorbar scale indicates the detrended bed elevation.

409 **4 Results**

410 4.1 Simulation of alluvial alternate bars (Run P1505)

411 Figure 2 shows the plan views of the evolution of detrended bed surface elevation in Run
412 P1505. The initial upstream bump (t = 0 h) deflects flow and sediment transport. The sediment
413 eroded from the bump forms the first bar and triggers the development of smaller bars
414 downstream (t = 2 - 4 h). The bars get larger and taller as they migrate downstream. When they
415 reach equilibrium, their downstream migration and growth rate vary slowly and become stable.
416 The initially flat alluvial bed, during the bedform formation and migration process, develops into
417 a clear pattern of alternate bars. The initial disturbance gradually spreads out by decreasing
418 height and stretching in the flow direction, prompting new bars to develop downstream (e.g.,
419 Figure 3 in Defina, 2003).

420 The longitudinal bed profiles and the bed elevation difference between the right- and left-
421 side walls from the numerical results (Figure 3) can be compared to the measured data at the
422 equilibrium state from Lanzoni (2000, Figure 1g) (Figure 4). Bar amplitudes are calculated as the
423 difference between the right and left side of the bed elevation, measured 20 cm from each side
424 wall (Figure 3a, b). The amplitude and wavelength are calculated using half the vertical and
425 twice the horizontal peak-to-peak distances of the detrended profile. The celerity of migrating

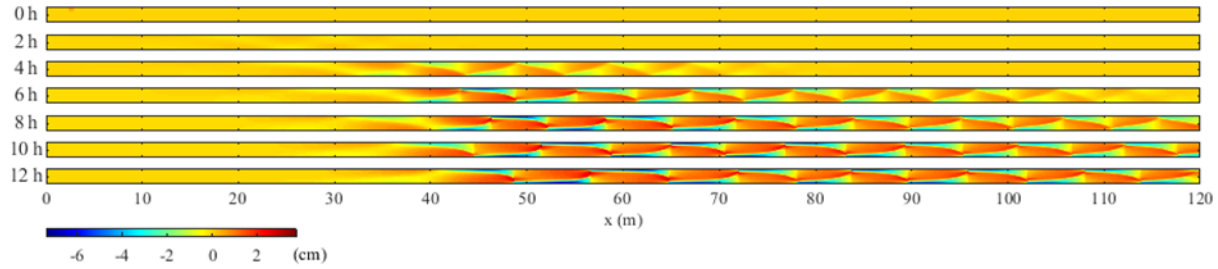

Figure 2. Detrended plan view of modeled bed evolution for the alluvial bar flume experiment (P1505) with the same longitudinal and transverse scale. Colorbar shows detrended bed elevation at the same scale for all plots.

426 bars is calculated by tracking topographic peaks over time. The longitudinal bed profiles from
427 numerical experiments exhibit highly ordered wave patterns. The axis bed profiles in the
428 numerical simulation and experiment indicate the transversally maximum value of bed elevation.

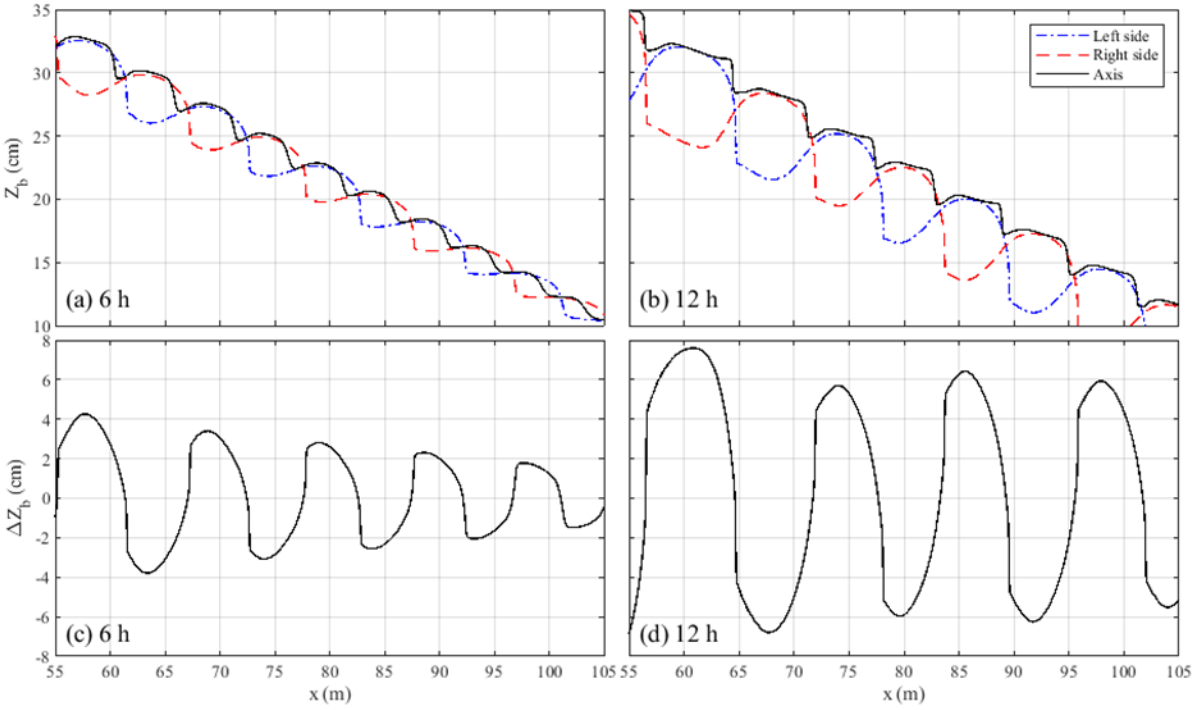

Figure 3. Modeled longitudinal bed profiles along the left- and right-side wall and axis at 6 h (a) and 12 h (b) and the difference between right- and left-side bed elevation at 6 h (c) and 12h (d).

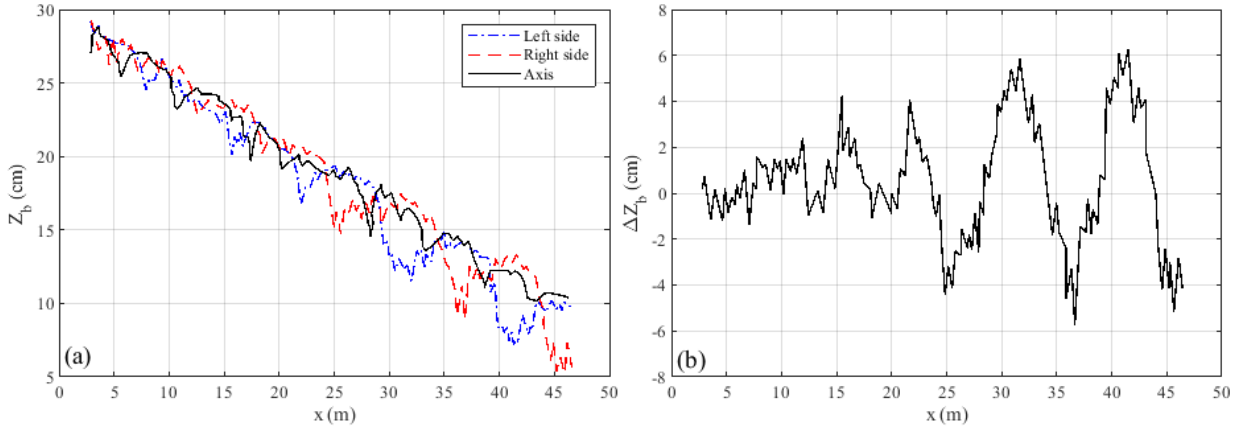

Figure 4. Measured (a) longitudinal bed profiles along the left- and right-side wall and (b) the difference between right- and left-side bed elevation at equilibrium (Figure 1g, Lanzoni, 2000).

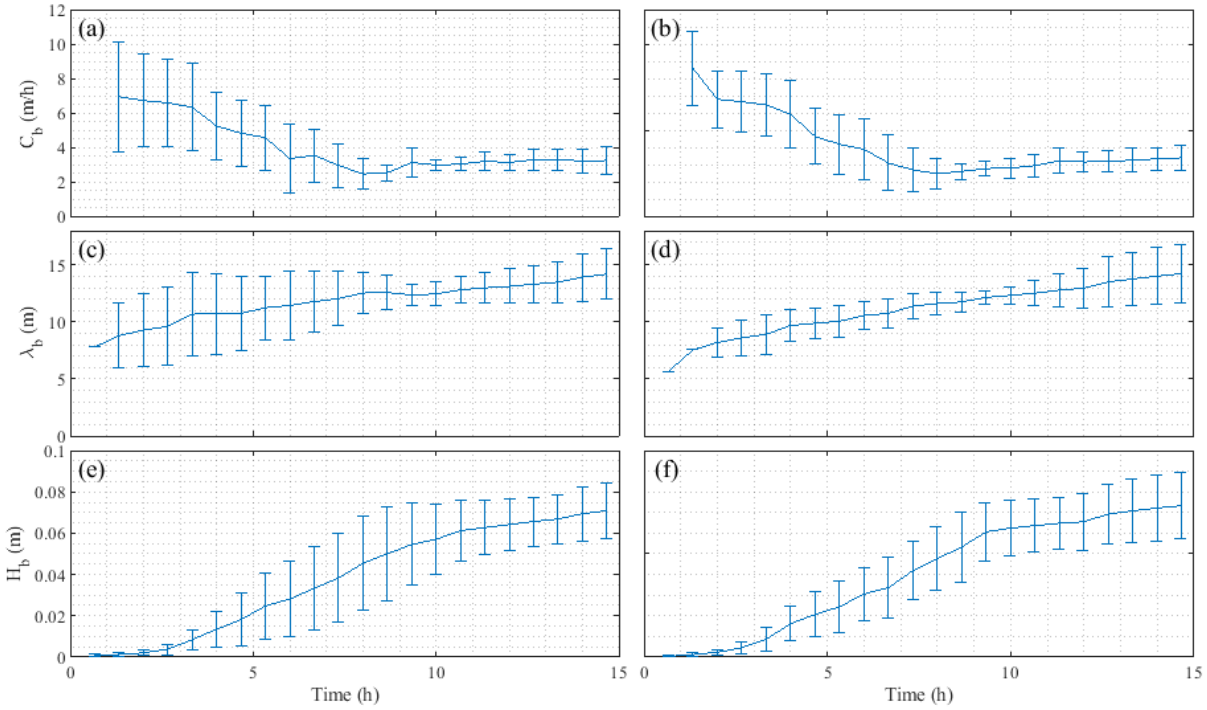

Figure 5. Computed time evolution of bar characteristics; celerity, wavelength, and amplitude (from top to bottom) on the left (a, c, and e) and right (b, d, and f) side of the channel.

Table 2. Comparison of Bar Characteristics from Measured Data and Computed Results.

	m/h	m	cm
Run	C_b	λ_b	H_b
P1505	2.8	10	7
Computed	3.2±0.5	14±2	7±1

As the calculated time changes in bar celerity (Figure 5a, b), wavelength (Figure 5c, d), and amplitude (Figure 5e, f) are small, and we consider the bed condition at near equilibrium. The mean characteristics of the bar (bar height, wavelength, and celerity) near equilibrium are compared and reported in Table 2. The computed bar wavelength, height, and celerity are approximately 14 m, 7 cm, and 3.2 m/s, respectively. The computed bar height and celerity show reasonably good agreement with observations of Lanzoni (2000), but the wavelength is slightly

435 overestimated. However, the computed alternate bar wavelength is approximately nine times the
436 channel width showing good agreement with Defina's (2003) numerical result and laboratory
437 data of alternate bar wavelength prediction (Ikeda, 1984).

438 4.2 Simulation of mixed bedrock-alluvial experiment (Run 2-B2)

439 Figure 6 shows a series of numerical results illustrating the time evolution of bed
440 configuration for the mixed bedrock-alluvial experiment (Run 2-B2) commencing from a 2 cm
441 thick alluvial cover (t = 0 h). The non-uniform sediment distribution, feeding more sediment at

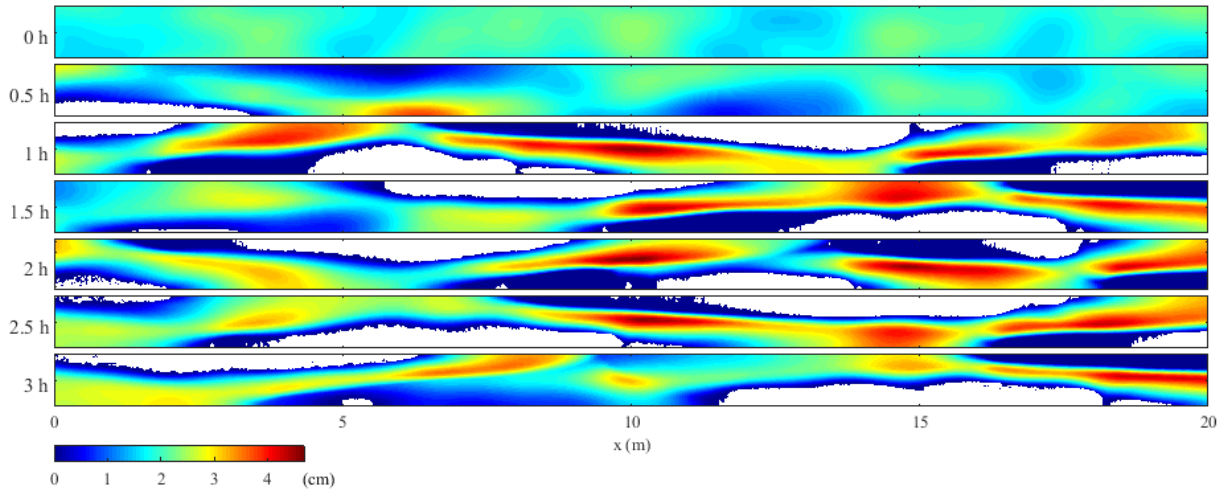

Figure 6. Simulated bed evolution of Run 2-B2. Colorbar shows the thickness of the sediment cover, and white areas correspond to the exposed bedrock surface.

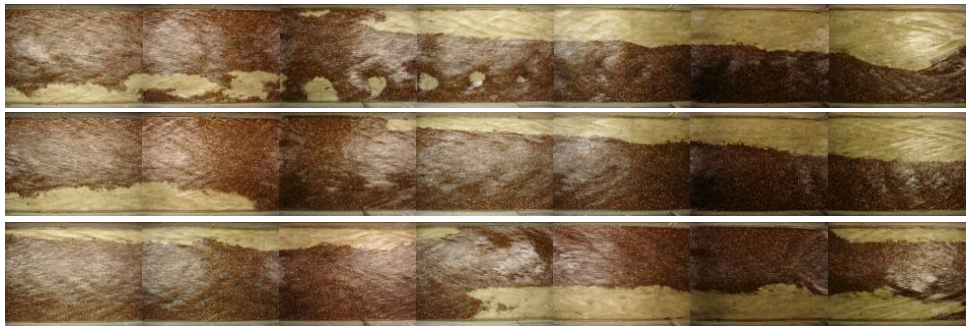

Figure 7. Time evolution of bedrock exposure Run 2-B4 at times are 1 ,4, and 7 hourse from top to bottom: Q_s= 97 g/s, q_s/q_c= 0.88, and P_c = 0.78 (Chatanantavet & Parker, 2008 (personal communication)). The channel is 0.9 m wide, 13 m long, water and sediment flow from left to right, and light and dark areas correspond to bedrock and sediment, respectively.

one side than the other, causes flow deflection induced by a laterally sloping bed at the upstream end (t = 0.5 h). At an early stage, this disturbance quickly erodes sediment on the right side of the channel down to the bedrock bed and creates pools and bars downstream. Then the exposed bedrock bed area, indicated as a white area, increases as the pools deepen and bars grow taller (t = 1 h). The sediment on the bed forms a strip of sediment shifting from one side to the other side of the channel through time while maintaining a consistent fraction of bedrock cover. Similar patterns were observed in the Chatanantavet and Parker (2008) experiments; for example, Figure 7 shows the time evolution of bedrock exposure from Run 2-B4 (Table 1 in Chatanantavet and Parker, 2008) with $Q_s = 97$ g/s, $q_s/q_c = 0.88$, and $P_c = 0.78$ at equilibrium phase. Again, a continuous band of sediment forms comparable to Figure 6. However, the sediment cover is more expansive, and the bed sediment shifting from one to the other side is less sensitive because of the higher sediment supply rate than what was provided in Run 2-B2 modeled here.

Figure 8 shows the computed flow variables, bed topography, and sediment transport capacity at equilibrium (t = 5h). The flow depth and velocity over the exposed bedrock area are higher than on the alluvial bed. However, calculated shear stress is lower in exposed bedrock areas due to the smaller roughness and higher flow depth. The critical dimensionless shear stress is generally higher on the alluvial bed but smaller over the lee side of the bedforms. The sediment transport capacity tends to be higher over the exposed bedrock surface and stoss side of the bedform and lower on lee slopes.

Figure 9 shows the time evolution of channel averaged fraction of bedrock exposure $F_e = 1 - P_c$, alluvial thickness, relative Shields parameter, and bedload transport rate. A ratio of alluvial coverage of bed surface in the area of interest determines the fraction of bedrock covered with sediment $P_c = A_c/A_t$ (Johnson, 2014), where A_c is the area covered with sediment and A_t

465 is the total area of interest, or numerically $P_c = \sum P_{ci} / N$, where P_{ci} is the local fraction of

466 bedrock cover (equation 8) and N is the total number of cells in the domain. The fraction of

467 bedrock exposure is initially zero when the bed is entirely covered by sediment and quickly

468 converges toward a near-equilibrium state where F_e is 0.4 at t = 1 h (Figure 9a). The numerical

469 result of the degree of bedrock exposure presents a similar value of F_e to the experimental

470 observation. The averaged sediment cover thickness over an alluvial area varies little in the range

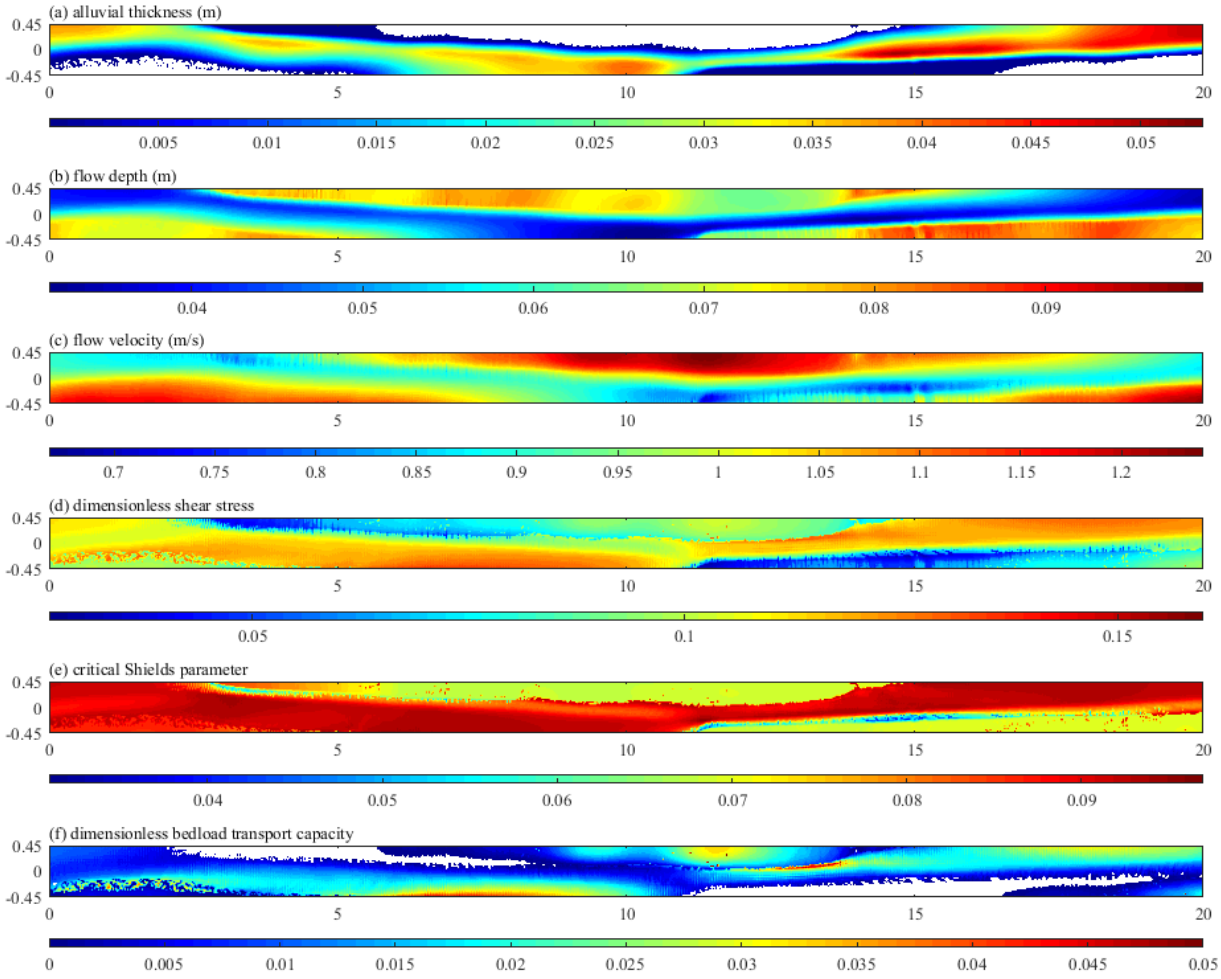

Figure 8. Plan view of (a) alluvial thickness, (b) flow depth. (c) flow velocity, (d) dimensionless shear stress, (e) critical Shields parameter, and (f) dimensionless bedload transport capacity at t = 5 h. Colorbars indicate the scale of computed values, respectively, and white areas correspond to (a) the exposed bedrock surface and (e) zero sediment transport rate.

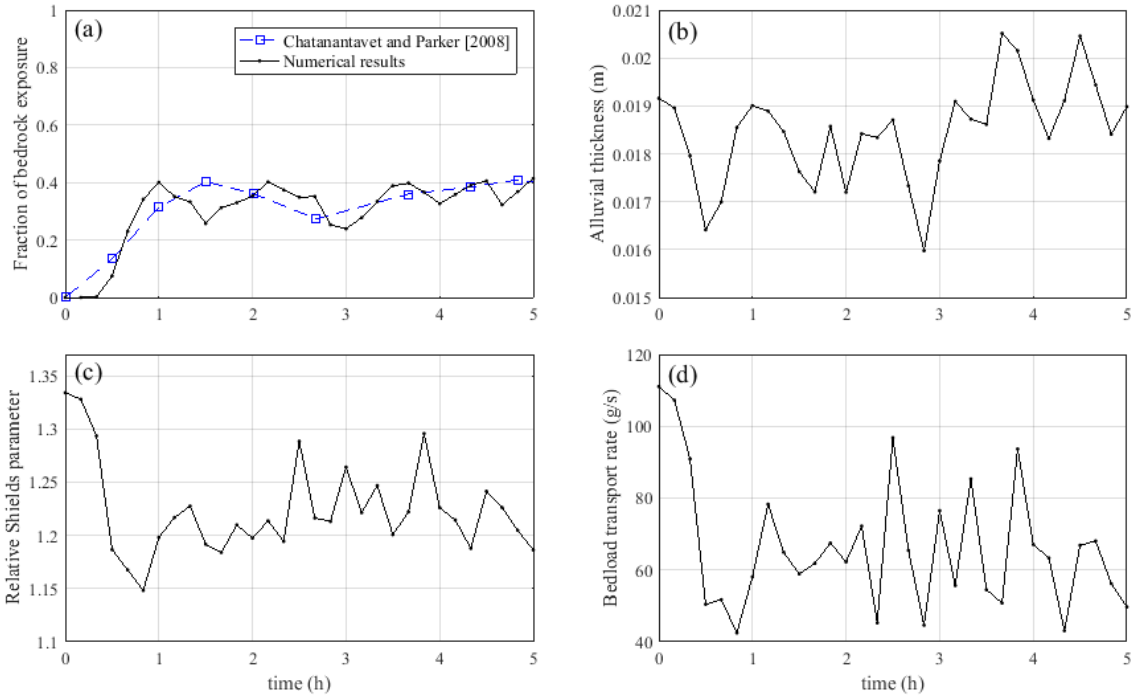

Figure 9. The time evolution of the (a) fraction of bedrock exposure from numerical and experimental results, (b) averaged alluvial thickness over the part of the bed covered with sediment, (c) relative Shields parameter, and(d) sediment transport rate.

of a single grain diameter (Figure 9b). The relative Shields parameter τ^* / τ_c^* (Figure 9c) and bedload transport rate (Figure 9d) decrease from an initially higher value to approximate equilibrium and vary around 1.2 and 70 g/s, respectively.

The comparison between the computed and measured quantities available from experimental observations is presented in Table 3. The agreement is reasonably good in predicting the fraction of bedrock cover, but higher flow depth and lower velocity in the experiment result in a lower Froude number and lower dimensionless shear stress. The model predicted lower shear stress over the bare bedrock areas than the alluvial areas because the bedform developed during the simulation. The alluvial bars form where flow depth is low and velocity is high, and pools exist over the bare bedrock area with deep flow depth and low velocity.

Table 3. Summary of Numerical Results

		cm	m/s		
Run	P_c	H	U	Fr	τ^*
2-B2 (C&P)[a]	0.59	5.5±1.5	1.11	1.51	0.11
2-B2[b]	0.60	6.0	1.00	1.32	0.10
2-B2 (covered zones) [c]		5.6	0.95	1.31	0.10
2-B2 (exposed zones) [d]		7.5	1.07	1.26	0.08

[a] Experimental results from Chatanantavet and Parker (2008).
[b] Reach averaged numerical results.
[c] Reach averaged numerical results only over the alluviated zones.
[d] Reach averaged numerical results only over the exposed bedrock zones.

5 Discussion

The present study shows the results that bed topography comparable to experimental observations from (1) free bar formation in a mild slope alluvial channel with fine grains (Lanzoni, 2000) and; (2) alluvial pattern in the mixed bedrock-alluvial channel in a steep slope channel with coarse grains (Chatanantavet & Parker, 2008). These suggest that the model can simulate complex flow and sediment transport to gain insight into mechanisms of the bedform development and alluviation patterns in mixed bedrock-alluvial channels.

The discrepancies between the numerical and experimental results are mainly associated with the initial and boundary conditions, which are not successfully reflected in the numerical models, such as the size of the initial disturbances and patterns of flow and sediment distribution at the channel inlet.

493 5.1 Discussion on ripple factor and form drag

494 Only a few studies have attempted to simulate sediment transport in a straight mixed
495 bedrock-alluvial channel using a 2D numerical model (Inoue et al., 2016; P. A. Nelson &
496 Seminara, 2012). These models estimated bed resistance to the flow using the grain roughness
497 and bedrock surface irregularity which is applicable to the plane bed. Our model includes the
498 effect of bed-form generation in roughness estimation since alternate bars often form in mixed
499 bedrock-alluvial channels (Chatanantavet & Parker, 2008; Inoue et al., 2016; P. A. Nelson &
500 Seminara, 2012). The hydraulic roughness height of alluvial bed changes according to the size of
501 bedforms (i.e., dunes and ripples) (Engelund, 1977; Raudkivi, 1997; van Rijn, 1982, 1984;
502 Vanoni & Hwang, 1967; Wiberg & Nelson, 1992).

503 Figure 10 shows the time evolution of bed topography with the same condition applied in
504 Run 2-B2 without including the bedform effect in the roughness calculation, and hence the
505 ineffective ripple factor. This simulation undergoes sediment washing out from the upstream end
506 of the channel while forming a bar-like bedform downstream. This result is comparable with the
507 results provided by Inoue et al. (2016).

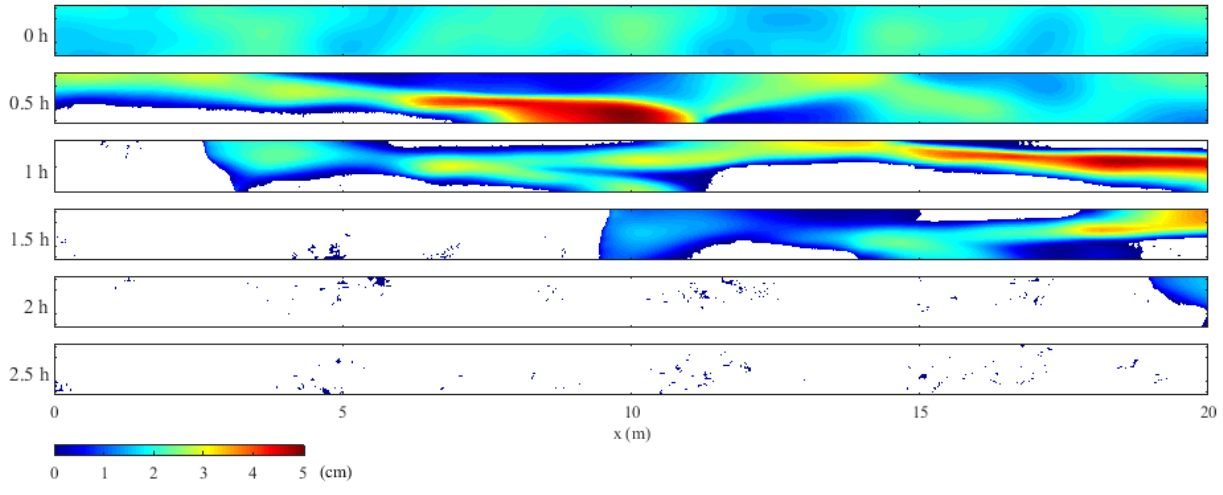

Figure 10. The time evolution of bed exposure for run 2-B2 without form drag effect ($k_f = 0$). Colorbar means alluvial cover thickness, and white area is exposed bedrock surface.

508 The prediction of bedload transport is based on the corrected dimensionless shear stress
509 for bedform roughness with a ripple factor (Meyer-Peter & Muller, 1948). The value of the
510 ripple factor has not been reported explicitly but empirically estimated as a ratio of grain shear
511 stress to the total bed shear stress (Ribberink, 1987; Vermeer, 1986). Nevertheless, the ripple
512 factor is often applied to sediment transport models to generate bedforms in alluvial channels
513 with a constant value of less than 1 (Defina, 2003; Van der Meer et al., 2011).

514 Figure 11 shows the plan view of the bed topography of Run 2-B2 without the
515 dimensionless shear stress correction by using a ripple factor equal to 1 in equation (16). The
516 upstream sediment erodes slower than the bed evolution in Figure 10, and the morphodynamic
517 process has enough time to form a longitudinal sediment strip because the form drag generates
518 higher flow resistance. However, larger dimensionless shear stress due to the absence of the
519 ripple factor in the supply-limited channel causes a thin layer of sediment at the upstream end
520 and a narrow strip of sediment. The strip of sediment is cut off at the narrowed section, and the
521 sediment is eventually washed out.

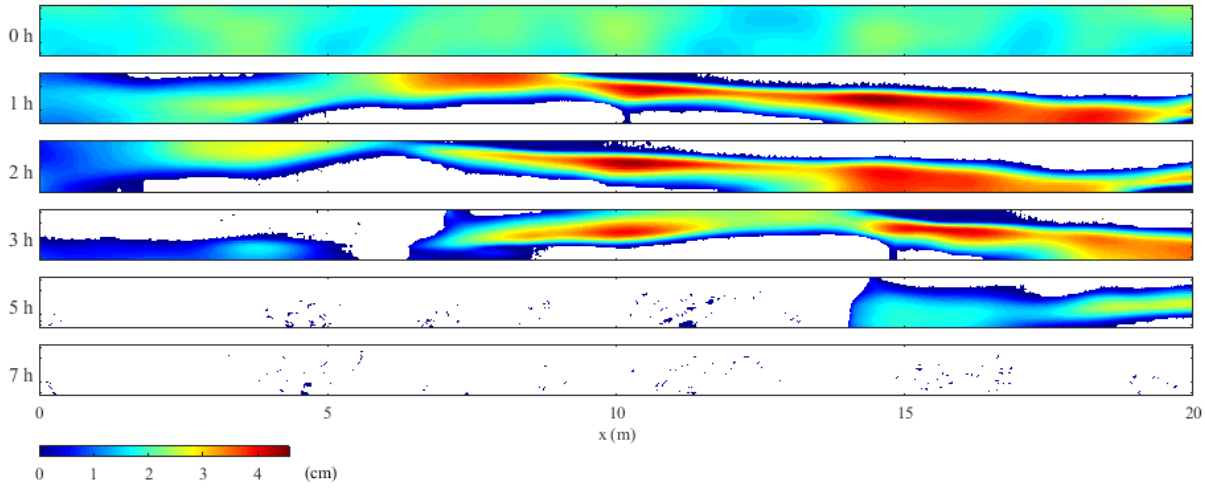

Figure 11. The time evolution of bed exposure for Run 2-B2 without ripple factor ($\mu = 1$). Colorbar indicates alluvial cover thickness, and the white area is exposed to the bedrock surface.

Comparing Figures 6 and 10-11, it can be seen that introducing both form drag to the roughness and ripple factor of the shear stress in bedload transport is critical in developing bedforms and persistent alluviation in bedrock channels where the sediment supply is less than the capacity of the channel. Results from previous models attempting to replicate these experiments (Inoue et al., 2014) show alternate bar development over the alluvial surface, but sediment supply less than the transport capacity decreases the thickness of the alluvial layer leading to sediment washing out from upstream and exposure of the entire bedrock.

The roughness component for form drag effectively increases drag and reduces flow velocity, whereas the ripple factor reduces shear stress in bedform-developed areas. Unlike the form drag acting on entire bedform fields, skin friction is responsible for the local bed surface roughness only. The smaller surface roughness over the exposed bedrock area than over the alluvial area produces higher shear stress. Therefore the model absent of form drag and ripple factor predicts a higher sediment transport rate as the fraction of sediment cover decreases in limited sediment supply conditions, resulting in a total washout of the sediment from the channel.

5.2 The impact of sediment transport roughness

Our model explicitly accounts for both the grain roughness and roughness produced by moving particles (Dietrich, 1982; Grant & Madsen, 1982; Smith & McLean, 1977; Wiberg & Rubin, 1989). To explore the importance of accounting for each of these components individually, we conducted a simulation where we ignored sediment transport roughness and increased the grain roughness to compensate for reduced bed roughness caused by the absence of sediment transport roughness.

Figure 12 shows the time evolution of bed topography for this simulation of Run 2-B2, excluding sediment transport roughness. A strip of sediment forms shifting from one side to the other side of the channel momentarily (t = 0.5 h), but then washes out from the upstream end of the channel (t = 2 h), with a small residual alluvial patch persisting only in a topographic low area in the bedrock (t = 4 h). The flow resistance decreases as bedrock gets exposed because of the underlying linear relationship between the fraction of bedrock cover and grain roughness. Unlike grain roughness, the sediment transport roughness is larger where grain movements actively take place. The sediment transport roughness tends to be higher over the bedrock surface partially covered with sediment because the sediment transport rate over the smoother bedrock surface, where the flow velocity is faster, is higher than over the rougher alluvial surface. The sediment transport roughness contributes to the formation of alluvial patches in the bedrock channel by reducing grain entrainment over the mixed bedrock-alluvial surface. These results indicate that separate accounting of grain and sediment transport roughness produces morphodynamic predictions that better match observations of persistent alluvial patterns in mixed bedrock-alluvial channels.

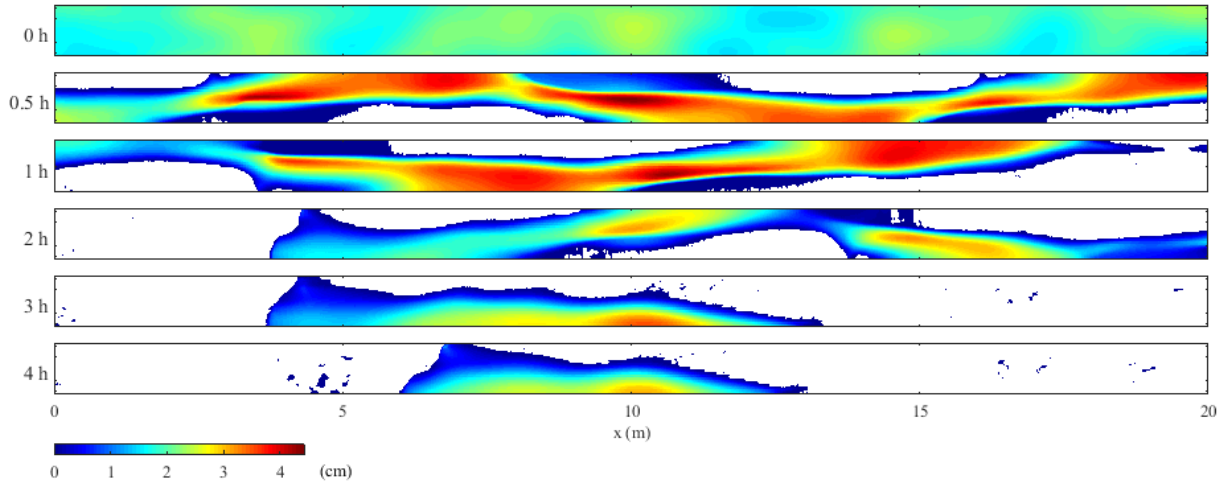

Figure 12. The time evolution of bed exposure for Run 2-B2 without sediment transport roughness from flow resistance (k_t = 0). Colorbar indicates alluvial cover thickness, and the white area is exposed to the bedrock surface.

6 Conclusions

In this study, we have developed a two-dimensional morphodynamic model to explore bar formation and migration in an alluvial channel and sediment transport mechanisms in a mixed bedrock-alluvial channel without sufficient sediment supply. Comparisons of model predictions with experimental observations from the free bar test show that the model predicts bed morphology and bedform development similar to the observations of the flume experiment. However, some discrepancies raise the need for proper tuning of model parameters and initial bottom perturbation.

The model predicts the flow field and sediment distribution patterns in mixed bedrock alluvial channels reasonably well. Numerical experiments show that the inclusion of bedform roughness and a shear stress correction for near-bed sediment transport is critical to be able to replicate the alluvial patterns over bare bedrock observed in flume experiments. The evolving interactions between the alluvial and bedrock bed surface, flow field, and sediment transport simultaneously modify the degree of sediment cover and bed topography. The numerical model presented in this study captures the behavior associated with the bedrock alluviation process and can be used to extend its applicability to various flow and sediment supply conditions with different channel slopes and antecedent topography.

Future work could explore the mechanisms of sediment pattern formation in mixed bedrock-alluvial rivers and characterize the effects of the channel slope, initial sediment cover thickness, difference between the grain and bedrock roughness, and bedrock configuration.

Acknowledgments

We thank Phairot Chatanantavet and Gary Parker for providing photographs of flume experiments.

Open Research

The code demonstrating the 2D morphodynamic model and numerical data of test cases shown herein are archived at https://github.com/rcemorpho/morph2d.

References

Ashida, K., & Michiue, M. (1972). Hydraulic Resistance of Flow in an Alluvia Bed and Bed Load Transport Rate. *Proceedings of Japan Society of Civil Engineers*, 59–69. https://scirp.org/reference/referencespapers.aspx?referenceid=1312271

Bernini, A., Caleffi, V., & Valiani, A. (2006). Numerical Modelling of Alternate Bars in Shallow Channels. *Braided Rivers*, 153–175. https://doi.org/10.1002/9781444304374.ch7

Chatanantavet, P., & Parker, G. (2008). Experimental study of bedrock channel alluviation under varied sediment supply and hydraulic conditions. *Water Resources Research*, *44*(12), 1–19. https://doi.org/10.1029/2007WR006581

De Vries M. (1965). Considerations about non-steady bed-load transport in open channels. *Proc. 11th Int. Congr. IAHR, Delft, the Netherlands, 3-8*.

Defina, A. (2003). Numerical experiments on bar growth. *Water Resources Research*, *39*(4), 1–12. https://doi.org/10.1029/2002WR001455

Demeter, G. I., Sklar, L. S., & Davis, J. R. (2005). The influence of variable sediment supply and bed roughness on the spatial distribution of incision in a laboratory bedrock channel. *2005 Fall Meeting of the AGU*, 2004.

Dietrich, W. E. (1982). Settling velocity of natural particles. *Water Resources Research*, *18*(6), 1615–1626. https://doi.org/10.1029/WR018i006p01615

603 Duan, J. G., & Julien, P. Y. (2005). Numerical simulation of the inception of channel
604 meandering. *Earth Surface Processes and Landforms*, *30*(9), 1093–1110.
605 https://doi.org/10.1002/esp.1264
606 Engelund, F. (1977). *Hydraulic resistance for flow over dunes.*
607 Finnegan, N. J., Sklar, L. S., & Fuller, T. K. (2007). Interplay of sediment supply, river incision,
608 and channel morphology revealed by the transient evolution of an experimental bedrock
609 channel. *Journal of Geophysical Research: Earth Surface*, *112*(3), 1–17.
610 https://doi.org/10.1029/2006JF000569
611 Gasparini, N. M., Whipple, K. X., & Bras, R. L. (2007). Predictions of steady state and transient
612 landscape morphology using sediment-flux-dependent river incision models. *Journal of*
613 *Geophysical Research: Earth Surface*, *112*(3), 1–20.
614 https://doi.org/10.1029/2006JF000567
615 Grant, W. D., & Madsen, O. S. (1982). Movable bed roughness in unsteady oscillatory flow.
616 *Journal of Geophysical Research*, *87*(C1), 469–481.
617 https://doi.org/10.1029/JC087iC01p00469
618 Hartshorn, K., Hovius, N., Dade, W. B., & Slingerland, R. L. (2002). Climate-driven bedrock
619 incision in an active mountain belt. *Science*, *297*(5589), 2036–2038.
620 https://doi.org/10.1126/science.1075078
621 Hodge, R. A., & Hoey, T. B. (2012). Upscaling from grain-scale processes to alluviation in
622 bedrock channels using a cellular automaton model. *Journal of Geophysical Research:*
623 *Earth Surface*, *117*(F1), n/a-n/a. https://doi.org/10.1029/2011JF002145

624 Hodge, R. A., & Hoey, T. B. (2016a). A Froude-scaled model of a bedrock-alluvial channel
625 reach: 1. Hydraulics. *Journal of Geophysical Research: Earth Surface*, *121*(9), 1578–
626 1596. https://doi.org/10.1002/2015JF003706
627 Hodge, R. A., & Hoey, T. B. (2016b). A Froude-scaled model of a bedrock-alluvial channel
628 reach: 2. Sediment cover. *Journal of Geophysical Research: Earth Surface*, *121*(9),
629 1597–1618. https://doi.org/10.1002/2015JF003709
630 Howard, A. D. (1980). Thresholds in river regimes. In *Thresholds in Geomorphology* (pp. 227–
631 258).
632 Howard, A. D. (1987). Modelling Fluvial Systems: Rock-, Gravel-, and Sand-bed Channels. In
633 *River Channels: Environment and Process* (pp. 69–94).
634 Howard, A. D. (1998). Long profile development of bedrock channels: Interaction of weathering,
635 mass wasting, bed erosion, and sediment transport. In K. J. Tinkler & E. E. Wohl (Eds.),
636 *Rivers Over Rock: Fluvial Processes in Bedrock Channels* (Volume 107, pp. 297–319).
637 https://doi.org/10.1029/GM107p0297
638 Howard, A. D., Dietrich, W. E., & Seidl, M. A. (1994). Modeling fluvial erosion on regional to
639 continental scales. *Journal of Geophysical Research: Solid Earth*, *99*(B7), 13971–13986.
640 https://doi.org/10.1029/94JB00744
641 Inoue, T., Iwasaki, T., Parker, G., Shimizu, Y., Izumi, N., Stark, C. P., & Funaki, J. (2016).
642 Numerical Simulation of Effects of Sediment Supply on Bedrock Channel Morphology.
643 *Journal of Hydraulic Engineering*, 04016014. https://doi.org/10.1061/(ASCE)HY.1943-
644 7900.0001124
645 Inoue, T., Izumi, N., Shimizu, Y., & Parker, G. (2014). Interaction among alluvial cover, bed
646 roughness, and incision rate in purely bedrock and alluvial-bedrock channel. *Journal of*

Geophysical Research: Earth Surface, *119*(10), 2123–2146. https://doi.org/10.1002/2014JF003133

Izumi, N., Yokokawa, M., & Parker, G. (2017). Incisional cyclic steps of permanent form in mixed bedrock-alluvial rivers. *Journal of Geophysical Research: Earth Surface*, *122*(1), 130–152. https://doi.org/10.1002/2016JF003847

Knighton, D. (2014). *Fluvial Forms and Processes*. Routledge. https://doi.org/10.4324/9780203784662

Lamb, M. P., Finnegan, N. J., Scheingross, J. S., & Sklar, L. S. (2015). New insights into the mechanics of fluvial bedrock erosion through flume experiments and theory. *Geomorphology*, *244*, 33–55. https://doi.org/10.1016/j.geomorph.2015.03.003

Lanzoni, S. (2000). Experiments on bar formation in a straight flume: 1. Uniform sediment. *Water Resources Research*, *36*(11), 3337–3349. https://doi.org/10.1029/2000WR900160

Luu, L. X., Egashira, S., & Takebayashi, H. (2004). Investigation of Tan Chau Reach In Lower Mekong Using Field Data And Numerical Simulation. *PROCEEDINGS OF HYDRAULIC ENGINEERING*, *48*(5), 1057–1062. https://doi.org/10.2208/prohe.48.1057

Maddux, T. B., McLean, S. R., & Nelson, J. M. (2003). Turbulent flow over three-dimensional dunes: 2. Fluid and bed stresses. *Journal of Geophysical Research: Earth Surface*, *108*(F1), n/a-n/a. https://doi.org/10.1029/2003jf000018

Maddux, T. B., Nelson, J. M., & McLean, S. R. (2003). Turbulent flow over three-dimensional dunes: 1. Free surface and flow response. *Journal of Geophysical Research: Earth Surface*, *108*(F1), n/a-n/a. https://doi.org/10.1029/2003JF000017

Mendoza, A., Abad, J. D., Langendoen, E. J., Wang, D., Tassi, P., & Abderrezzak, K. E. K. (2017). Effect of Sediment Transport Boundary Conditions on the Numerical Modeling

of Bed Morphodynamics. *Journal of Hydraulic Engineering*, *143*(4), 04016099. https://doi.org/10.1061/(ASCE)HY.1943-7900.0001208

Meyer-Peter, E., & Müller, R. (1948). Formulas for Bed-Load Transport. *Proceedings of the 2nd Meeting of the International Association of Hydraulic Research*, 39–64. https://doi.org/1948-06-07

Mishra, J., & Inoue, T. (2020). Alluvial cover on bedrock channels: applicability of existing models. *Earth Surface Dynamics*, *8*(3), 695–716. https://doi.org/10.5194/esurf-8-695-2020

Murray, A. B., & Paola, C. (1997). Properties of a cellular braided-stream model. *Earth Surface Processes and Landforms*, *22*(11), 1001–1025. https://doi.org/10.1002/(SICI)1096-9837(199711)22:11<1001::AID-ESP798>3.0.CO;2-O

Nelson, J. M., Bennett, J. P., & Wiele, S. M. (2003). Flow and sediment-transport modeling. *Tools in Fluvial Geomorphology*. https://doi.org/10.1002/0470868333.ch18

Nelson, J. M., & Smith, J. D. (1989). Mechanics of flow over ripples and dunes. *Journal of Geophysical Research*, *94*(C6), 8146. https://doi.org/10.1029/JC094iC06p08146

Nelson, P. A., Bolla Pittaluga, M., & Seminara, G. (2014). Finite amplitude bars in mixed bedrock-alluvial channels. *Journal of Geophysical Research: Earth Surface*, *119*(3), 566–587. https://doi.org/10.1002/2013JF002957

Nelson, P. A., McDonald, R. R., Nelson, J. M., & Dietrich, W. E. (2015a). Coevolution of bed surface patchiness and channel morphology: 1. Mechanisms of forced patch formation. *Journal of Geophysical Research F: Earth Surface*, *120*(9), 1687–1707. https://doi.org/10.1002/2014JF003428

692 Nelson, P. A., McDonald, R. R., Nelson, J. M., & Dietrich, W. E. (2015b). Coevolution of bed
693 surface patchiness and channel morphology: 2. Numerical experiments. *Journal of*
694 *Geophysical Research F: Earth Surface*, *120*(9), 1708–1723.
695 https://doi.org/10.1002/2014JF003429
696 Nelson, P. A., & Seminara, G. (2012). A theoretical framework for the morphodynamics of
697 bedrock channels. *Geophysical Research Letters*, *39*(6), 1–7.
698 https://doi.org/10.1029/2011GL050806
699 Nittrouer, J. A., Mohrig, D., Allison, M. A., & Peyret, A. P. B. (2011). The lowermost
700 Mississippi River: A mixed bedrock-alluvial channel. *Sedimentology*, *58*(7), 1914–1934.
701 https://doi.org/10.1111/j.1365-3091.2011.01245.x
702 Parker, G., & Klingeman, P. C. (1982). On why gravel bed streams are paved. *Water Resources*
703 *Research*, *18*(5), 1409–1423. https://doi.org/10.1029/WR018i005p01409
704 Parker, G., & Toro-Escobar, C. M. (2002). Equal mobility of gravel in streams: The remains of
705 the day. *Water Resources Research*, *38*(11), 46-1-46–48.
706 https://doi.org/10.1029/2001wr000669
707 Qian, H., Cao, Z., Liu, H., & Pender, G. (2017). Numerical modelling of alternate bar formation,
708 development and sediment sorting in straight channels. *Earth Surface Processes and*
709 *Landforms*, *42*(4), 555–574. https://doi.org/10.1002/esp.3988
710 Raudkivi, A. J. (1997). Ripples on Stream Bed. *Journal of Hydraulic Engineering*, *123*(1), 58–
711 64. https://doi.org/10.1061/(ASCE)0733-9429(1997)123:1(58)
712 Ribberink, J. S. (1987). Mathematical modelling of one-dimensional morphological changes in
713 rivers with non-uniform sediment. *Communications on Hydraulic & Geotechnical*
714 *Engineering - Delft University of Technology*, *87–2*.

715 Schuurman, F., Marra, W. A., & Kleinhans, M. G. (2013). Physics-based modeling of large
716 braided sand-bed rivers: Bar pattern formation, dynamics, and sensitivity. *Journal of*
717 *Geophysical Research: Earth Surface*, *118*(4), 2509–2527.
718 https://doi.org/10.1002/2013JF002896
719 Seidl, M., & Dietrich, W. (1992). The problem of channel erosion into bedrock. *Catena*,
720 *23*(Supplement), 101–104.
721 Sklar, L., & Dietrich, W. (1998). River longitudinal profiles and bedrock incision models:
722 Stream power and the influence of sediment supply. In K. J. Tinkler & E. E. Wohl (Eds.),
723 *Rivers Over Rock: Fluvial Processes in Bedrock Channels* (Volume 107, pp. 237–260).
724 https://doi.org/10.1029/GM107p0237
725 Sklar, L., & Dietrich, W. (2001). Sediment and rock strength controls on river incision into
726 bedrock. *Geology*, *29*(12), 1087. https://doi.org/10.1130/0091-
727 7613(2001)029<1087:SARSCO>2.0.CO;2
728 Sklar, L., & Dietrich, W. (2004). A mechanistic model for river incision into bedrock by
729 saltating bed load. *Water Resources Research*, *40*(6), 1–21.
730 https://doi.org/10.1029/2003WR002496
731 Smith, J. D., & Mclean, S. R. (1984). A Model for Flow in Meandering Streams. *Water*
732 *Resources Research*, *20*(9), 1301–1315. https://doi.org/10.1029/WR020i009p01301
733 Smith, J. D., & McLean, S. R. (1977). Spatially averaged flow over a wavy surface. *Journal of*
734 *Geophysical Research*, *82*(12), 1735. https://doi.org/10.1029/JC082i012p01735
735 Soulsby, R. (1997). Dynamics of Marine Sands. In *Dynamics of Marine Sands*. Thomas Telford
736 Ltd. https://doi.org/10.1680/DOMS.25844

737 Stansby, P. (2003). A mixing-length model for shallow turbulent wakes. *Journal of Fluid*
738 *Mechanics*, *495*, 369–384. https://doi.org/10.1017/S0022112003006384
739 Struiksma, N. (1985). Prediction of 2-D bed topography in rivers. *Journal of Hydraulic*
740 *Engineering*, *111*(8), 1169–1182. https://doi.org/10.1061/(ASCE)0733-
741 9429(1985)111:8(1169)
742 Talmon, A. M., Struiksma, N., & Van Mierlo, M. C. L. M. (1995). Laboratory measurements of
743 the direction of sediment transport on transverse alluvial-bed slopes. *Journal of*
744 *Hydraulic Research*, *33*(4), 495–517. https://doi.org/10.1080/00221689509498657
745 Tinkler, K., & Wohl, E. (1998). A Primer on Bedrock Channels. In K. Tinkler & E. Wohl (Eds.),
746 *Rivers Over Rock: Fluvial Processes in Bedrock Channels* (Vol. 107, pp. 1–18).
747 Blackwell Publishing Ltd. https://doi.org/10.1029/GM107P0001
748 Toro, E. F. (2009). The HLL and HLLC Riemann Solvers. In *Riemann Solvers and Numerical*
749 *Methods for Fluid Dynamics* (pp. 315–344). Springer Berlin Heidelberg.
750 https://doi.org/10.1007/b79761_10
751 Turowski, J. M., Hovius, N., Meng-Long, H., Lague, D., & Men-Chiang, C. (2008). Distribution
752 of erosion across bedrock channels. *Earth Surface Processes and Landforms*, *33*(3), 353–
753 363. https://doi.org/10.1002/esp.1559
754 Turowski, J. M., Hovius, N., Wilson, A., & Horng, M. J. (2008). Hydraulic geometry, river
755 sediment and the definition of bedrock channels. *Geomorphology*, *99*(1–4), 26–38.
756 https://doi.org/10.1016/j.geomorph.2007.10.001
757 Turowski, J. M., Lague, D., & Hovius, N. (2007). Cover effect in bedrock abrasion: A new
758 derivation and its implications for the modeling of bedrock channel morphology. *Journal*

759 *of Geophysical Research: Earth Surface*, *112*(4), 1–16.
760 https://doi.org/10.1029/2006JF000697
761 Van der Meer, C., Mosselman, E., Sloff, K., Jager, B., Zolezzi, G., & Tubino, M. (2011).
762 Numerical simulations of upstream and downstream overdeepening. *River, Coastal and*
763 *Estuarine Morphodynamics*, *1967*, 1721–1729.
764 van Rijn, L. C. (1982). Equivalent Roughness of Alluvial Bed. *Journal of the Hydraulics*
765 *Division*, *108*(10), 1215–1218. https://doi.org/10.1061/JYCEAJ.0005917
766 van Rijn, L. C. (1984). Sediment Transport, Part II: Suspended Load Transport. *Journal of*
767 *Hydraulic Engineering*, *110*(11), 1613–1641. https://doi.org/10.1061/(ASCE)0733-
768 9429(1984)110:11(1613)
769 Vanoni, V. A., & Hwang, L.-S. (1967). Relation Between Bed Forms and Friction in Streams.
770 *Journal of the Hydraulics Division*, *93*(3), 121–144.
771 https://doi.org/10.1061/jyceaj.0001607
772 Vermeer, K. (1986). The ripple factor in sediment transport equations. *Rep. R657/M1314-V*.
773 Whipple, K. X. (2001). Fluvial Landscape Response Time: How Plausible Is Steady-State
774 Denudation? *American Journal of Science*, *301*(4–5), 313–325.
775 https://doi.org/10.2475/ajs.301.4-5.313
776 Whipple, K. X. (2004). Bedrock rivers and the geomorphology of active orogens. In *Annual*
777 *Review of Earth and Planetary Sciences* (Vol. 32, Issue 1, pp. 151–185).
778 https://doi.org/10.1146/annurev.earth.32.101802.120356
779 Whipple, K. X., & Tucker, G. E. (1999). Dynamics of the stream-power river incision model:
780 Implications for height limits of mountain ranges, landscape response timescales, and

781 research needs. *Journal of Geophysical Research: Solid Earth*, *104*(B8), 17661–17674.
782 https://doi.org/10.1029/1999JB900120
783 Whipple, K. X., & Tucker, G. E. (2002). Implications of sediment-flux-dependent river incision
784 models for landscape evolution. *Journal of Geophysical Research*, *107*(B2), 2039.
785 https://doi.org/10.1029/2000JB000044
786 Wiberg, P. L., & Nelson, J. M. (1992). Unidirectional flow over asymmetric and symmetric
787 ripples. *Journal of Geophysical Research*, *97*(C8), 12745.
788 https://doi.org/10.1029/92JC01228
789 Wiberg, P. L., & Rubin, D. M. (1989). Bed roughness produced by saltating sediment. *Journal of*
790 *Geophysical Research*, *94*(C4), 5011. https://doi.org/10.1029/JC094iC04p05011
791 Wiberg, P. L., & Smith, J. D. (1987). Calculations of the critical shear stress for motion of
792 uniform and heterogeneous sediments. *Water Resources Research*, *23*(8), 1471–1480.
793 https://doi.org/10.1029/WR023i008p01471
794 Wohl, E. E. (1993). Bedrock Channel Incision along Piccaninny Creek, Australia. *The Journal of*
795 *Geology*, *101*(6), 749–761. https://doi.org/10.1086/648272
796 Wu, F. C., Shao, Y. C., & Chen, Y. C. (2011). Quantifying the forcing effect of channel width
797 variations on free bars: Morphodynamic modeling based on characteristic dissipative
798 Galerkin scheme. *Journal of Geophysical Research: Earth Surface*, *116*(3), 1–20.
799 https://doi.org/10.1029/2010JF001941
800 Zhang, L., Parker, G., Stark, C. P., Inoue, T., Viparelli, E., Fu, X., & Izumi, N. (2015). Macro-
801 roughness model of bedrock-alluvial river morphodynamics. *Earth Surface Dynamics*,
802 *3*(1), 113–138. https://doi.org/10.5194/esurf-3-113-2015

803 Zhang, L, Iwasaki, T., Li, T., Fu, X., Wang, G., & Parker, G. (2019). Bedrock-alluvial streams
804 with knickpoint and plunge pool that migrate upstream with permanent form. *Scientific*
805 *Reports*, *9*(1), 1–9. https://doi.org/10.1038/s41598-019-42389-2
806 Zhang, L, Stark, C., Schumer, R., Kwang, J., Li, T., Fu, X., Wang, G., & Parker, G. (2018). The
807 Advective-Diffusive Morphodynamics of Mixed Bedrock-Alluvial Rivers Subjected to
808 Spatiotemporally Varying Sediment Supply. *Journal of Geophysical Research: Earth*
809 *Surface*, *123*(8), 1731–1755. https://doi.org/10.1029/2017JF004431